

Deciphering and integrating invariants for neural operator learning with various physical mechanisms

Rui Zhang¹, Qi Meng², and Zhi-Ming Ma¹

¹Academy of Mathematics and Systems Science, Chinese Academy of Sciences (CAS), Beijing 100190, China

²Microsoft Research, Beijing 100080, China

E-mails: rayzhang@amss.ac.cn, meq@microsoft.com

Abstract

Neural operators have been explored as surrogate models for simulating physical systems to overcome the limitations of traditional partial differential equation (PDE) solvers. However, most existing operator learning methods assume that the data originate from a single physical mechanism, limiting their applicability and performance in more realistic scenarios. To this end, we propose Physical Invariant Attention Neural Operator (PIANO) to decipher and integrate the physical invariants (PI) for operator learning from the PDE series with various physical mechanisms. PIANO employs self-supervised learning to extract physical knowledge and attention mechanisms to integrate them into dynamic convolutional layers. Compared to existing techniques, PIANO can reduce the relative error by 13.6%-82.2% on PDE forecasting tasks across varying coefficients, forces, or boundary conditions. Additionally, varied downstream tasks reveal that the PI embeddings deciphered by PIANO align well with the underlying invariants in the PDE systems, verifying the physical significance of PIANO. The source code will be publicly available at: <https://github.com/optray/PIANO>.

1 INTRODUCTION

Partial differential equations (PDEs) provide a fundamental mathematical framework to describe a wide range of natural phenomena and physical processes, such as fluid dynamics [32], life science [38], and quantum mechanics [23], among others. Accurate and efficient solutions of PDEs are essential for understanding and predicting the behavior of these physical systems. However, due to the inherent complexity of PDEs, analytical solutions are often unattainable, necessitating the development of numerical methods for their approximation [26]. Over the years, numerous numerical techniques have been proposed for solving PDEs, such as the finite difference method, finite element method, and spectral method [43]. These methods have been widely used in practice, providing valuable insights into the behavior of complex systems governed by PDEs [8; 39]. Despite the success of classical numerical methods in solving a wide range of PDEs, there are several limitations associated with these techniques, such as the restriction on step size, difficulties in handling complex geometries, and curse of dimensionality for high dimensional PDEs [1; 13; 22].

In recent years, machine learning (ML) methods have evolved as a disruptive technology to classical numerical methods for solving scientific calculation problems for PDEs. By leveraging the power of data-driven techniques or the expression ability of neural networks, ML-based methods have the potential to overcome some of the shortcomings of traditional numerical approaches [7; 11; 13; 34; 35; 50]. In particular, by using the deep neural network to represent the solution of the PDE, ML methods can efficiently handle complex geometries and solve high dimensional PDEs [17]. The representative works include the DeepBSDE method, which can solve parabolic PDEs in 100 dimensions [13]; the random feature model, which can easily handle complex geometries and achieve spectral accuracy [3]; the ML-based reduced order modeling, which can improve the accuracy and efficiency of traditional reduced-order modeling for nonlinear problems [5; 10; 48]. However, these methods are applied to the fixed initial field (or external force field), and they require the retraining of neural networks when solving the PDEs with changing high-dimensional initial fields.

In addition to these developments, neural operators have emerged as a more promising approach to simulate physical systems with deep learning, using neural networks as surrogate models to learn the PDE operator between functional spaces from data [18; 22; 25], which can significantly accelerate the simulation process. Most studies along this line focus on the network architecture design to ensure both simulation accuracy and inference efficiency. For example, DeepONet [25] and its variants [19; 37; 46], Fourier neural operators [22; 33; 45], and transformers-based operators [2; 21] are proposed to respectively deal with continuous input and output space, different frequency components, and complex geometries. Compared to traditional methods, neural operators break the restriction on spatiotemporal discretization and enjoy a speed up of thousands of times, demonstrating enormous potential in areas such as inverse design and physical simulations, among others [20; 22]. However, these methods only consider PDEs generated from a single formula by default, limiting the applicability of neural operators to multi-physical scenarios, e.g., datasets of the PDE systems sampled under different conditions (boundary conditions, parameters, etc.).

To address this issue, message passing neural networks (MPNN) incorporate the indicator of the scenario (i.e., the PDE parameters) into inputs to improve the generalization capabilities of the model [1]. DyAd supervised learns the physical information through an encoder and automatically adapts them to different scenarios [47]. Although incorporating the physical knowledge can enhance the performance of the neural operator, these methods still require access to the high-level PDE information in the training or test stage [1; 47]. However, in many real-world applications, collecting high-level physical information that governs the behavior of PDE systems can be infeasible or prohibitively expensive. For example, in fluid dynamics or ocean engineering, scientists can gather numerous flow field data controlled by varying and unknown Reynolds numbers, and calculating them would require numerous calls to PDE solvers [28; 35].

To this end, we propose the Physical Invariant Attention Neural Operator (PIANO), a novel operator learning framework for deciphering and integrating physical knowledge from PDE series with various physical invariants (PIs), such as varying coefficients and boundary conditions. PIANO has two branches: a PI encoder that extracts physical invariants and a personalized operator that predicts the complementary field representation of each PDE system (Fig. 1.a). As illustrated in Fig. 1, PIANO employs two key designs: the contrastive learning stage for learning the PI encoder and an attention mechanism to incorporate this knowledge into neural operators through dynamic convolutional layers (DyConv) [6]. On the one hand, contrastive learning extracts the PI representation through the similarity loss defined on augmented spatiotemporal patches cropped from the dataset (Fig. 1.b). To enhance consistency with physical priors, we propose three physics-aware cropping techniques to adapt different PI properties for different PDE systems, such as spatiotemporal invariant, boundary invariant, etc. (Fig. 1.b.iii). This physics-aware contrastive learning technique extracts the PI representation without the need for the labels of the PDE conditions, thus providing the corresponding PI information for each PDE series (Fig. 1.b). On the other hand, after the PI encoder is learned by contrastive learning, we compute attention (i.e., a_k^i in Fig. 1.c) of the PI representation extracted by the PI encoder and reweight the convolutional kernel in the DyConv layer to obtain a personalized operator (Fig. 1.c). This personalized operator, incorporated with the PI information as an indicator of the PDE condition, can predict the evolution of each PDE field in a mixed dataset with guaranteed generalization performance.

We demonstrate our method’s effectiveness and physical meaning on several benchmark problems, including Burgers’ equation, convection-diffusion equation (CDE), and Navier-Stokes equation (NSE). Our results show that PIANO achieves superior accuracy and generalization compared to existing methods for solving PDEs with various physical mechanisms. According to the results of four experiments, PIANO can reduce the relative error rate by 15.1%-82.2% by deciphering and integrating the PIs of PDE systems. Furthermore, we conduct experiments to evaluate the quality of PI embedding through some downstream tasks, such as unsupervised dimensionality reduction and supervised classification (regression). These results indicate that the manifold structures of PI embeddings align well with the underlying PIs hidden in the PDE series (e.g., Reynolds numbers in NSE and external forces in Burgers’ equation), thereby enjoying the physical significance.

2 THE FRAMEWORK OF PIANO

In this section, we introduce the framework of PIANO, including how PIANO deciphers PIs from unlabeled multi-physical datasets and the procedure to incorporate them into the neural operator.

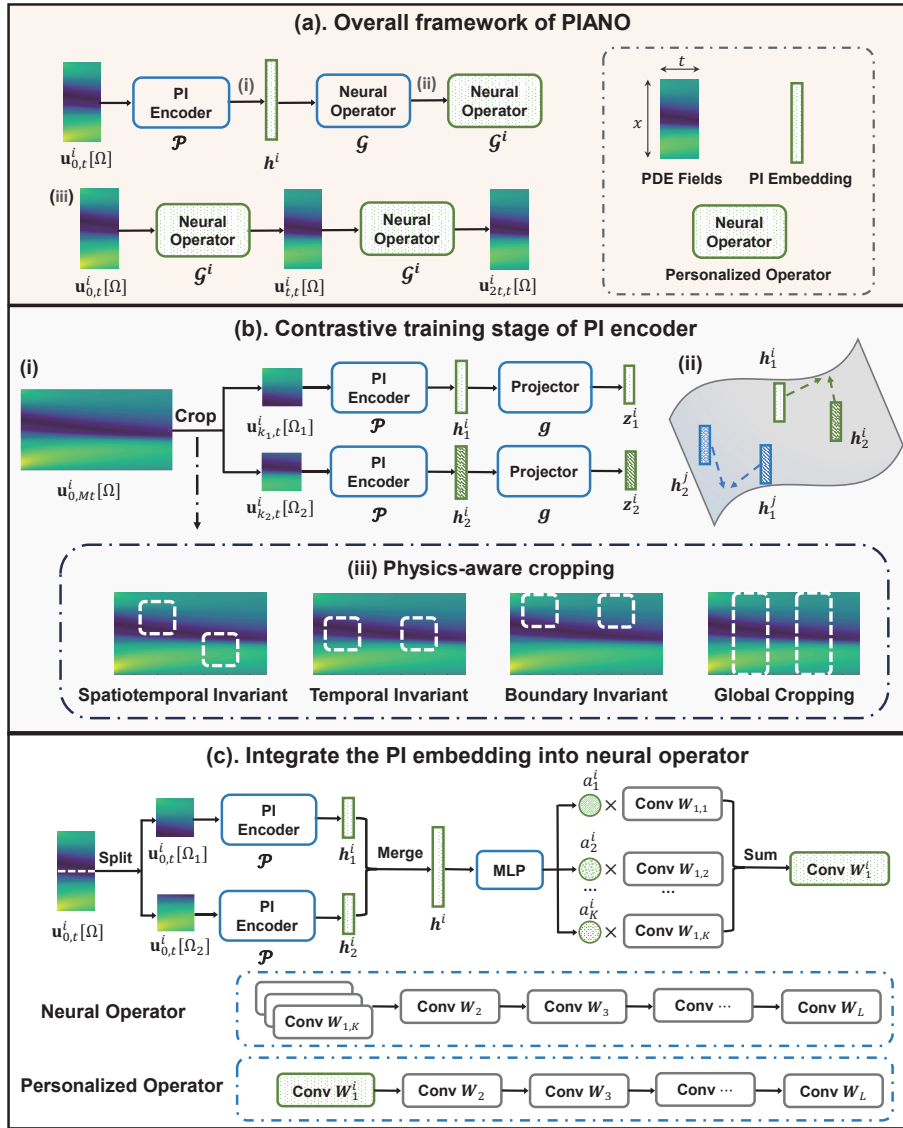


Figure 1: **The illustration of PIANO.** (a). **The overall framework for PIANO when forecasting the PDE series.** Given the i -th PDE initial fields $\mathbf{u}_{0,t}^i[\Omega]$, PIANO first infers the PI embedding h^i via the PI encoder \mathcal{P} , and then integrate h^i into neural operator \mathcal{G} to obtain a personalized operator \mathcal{G}^i for \mathbf{u}^i . After that, PIANO predicts the subsequent PDE fields with this personalized operator. (b). **Training stage of PI encoder.** (i). Illustration of contrastive learning. We crop two patches from each PDE series in a mini-batch according to the physical priors. The PI encoder and the projector are trained to maximize the similarity of two homologous patches. (ii). The effect of SimCLR loss, which brings closer (pushes apart) the representations governed by the same (different) physical parameters. (iii). Physics-aware cropping strategy of contrastive learning in PIANO. The cropping strategy should align with the physical prior of the PDE system. We illustrate the cropping strategies for spatiotemporal, temporal, and boundary invariants. We also represent the global cropping strategy for comparison, which does not consider the more detailed physical priors and feeds the entire spatial fields directly. (c). **Integrate the PI representation.** We use a split-merge trick to obtain the PI embedding h^i for the PDE field \mathbf{u}^i , and feed h^i into a multi-layer perception (MLP) to obtain K non-negative scales $\{a_k^i\}_{k=1}^K$ with $\sum_k a_k^i = 1$. We use a_k^i as the attention to reweight the DyConv layer in the neural operator and thus obtain a personalized operator for \mathbf{u}^i , which is incorporated with physical knowledge in h^i .

2.1 Description on the PDE system

Consider the time-dependent PDE system, which can be expressed as follows:

Table 1: Examples of three types of PIs on 1D heat equations ($\Omega = [-1, 1]$).

Formula of the PDE	Type of PI	PI θ	PI space Θ
$\partial_t u = \kappa \Delta u, u(\pm 1, t) = 0$	spatiotemporal invariant	κ	$[0, 1]$
$\partial_t u = 0.1 \Delta u + f(x), u(\pm 1, t) = 0$	temporal invariant	$f(x)$	$\{a \sin(x) : a \in [0, 1]\}$
$\partial_t u = 0.1 \Delta u, u(\pm 1, t) = c$	boundary invariant	c	$[-1, 1]$

$$\begin{cases} \partial_t u = \mathcal{R}(u, \theta_{\mathcal{R}}), \\ u(\mathbf{x}, 0) = u_0(\mathbf{x}), \\ \mathcal{B}[u](\mathbf{x}, t, \theta_{\mathcal{B}}) = 0, \end{cases} \quad (\mathbf{x}, t) \in \Omega \times [0, T], \quad (1)$$

where \mathcal{R} is the differential operator with parameter $\theta_{\mathcal{R}} \in \Theta_{\mathcal{R}}$, Ω is a bounded domain, and u_0 represents the initial conditions. Let $\mathcal{B}[u]$ be the boundary condition governed by the parameter $\theta_{\mathcal{B}} \in \Theta_{\mathcal{B}}$. Let $\Theta := \Theta_{\mathcal{R}} \times \Theta_{\mathcal{B}}$ be the product space between $\Theta_{\mathcal{R}}$ and $\Theta_{\mathcal{B}}$, and $\theta := (\theta_{\mathcal{R}}, \theta_{\mathcal{B}}) \in \Theta$ be the global parameters of the PDE system. We utilize $\mathbf{u}_{k,t}[\Omega] := [u_k[\Omega], \dots, u_{k+t-1}[\Omega]]$ to denote the t frame ($t \in \mathbb{N}^+$) PDE series defined in Ω .

In this paper, we consider the scenario where $\theta \in \Theta$ is a time-invariant parameter. In other words, the parameters θ that govern the PDE system in Eq. 1 do not change over time, which includes the following three scenarios:

- Spatiotemporal invariant: $\mathbf{u}_{k_1,t}[\Omega_1]$ and $\mathbf{u}_{k_2,t}[\Omega_2]$ share the same $\theta_{\mathcal{R}}$ for all $k_1, k_2 \in [0, T]$ and $\Omega_1, \Omega_2 \subset \Omega$.
- Temporal invariant: Given $\Omega' \subset \Omega$, $\mathbf{u}_{k_1,t}[\Omega']$ and $\mathbf{u}_{k_2,t}[\Omega']$ share the same $\theta_{\mathcal{R}}$ for all $k_1, k_2 \in [0, T]$.
- Boundary invariant: $\mathbf{u}_{k_1,t}[\Omega]$ and $\mathbf{u}_{k_2,t}[\Omega]$ share the same $\theta_{\mathcal{B}}$ for all $k_1, k_2 \in [0, T]$.

In Table 1, we give some examples of 1D heat equations to illustrate the above three types of PIs.

2.2 The learning regime

Given the t frame PDE series $\mathbf{u}_{k,t}[\Omega]$ governed by Eq. 1, an auto-regressive neural operator \mathcal{G} acts as a surrogate model, which produces the next t frame PDE solution as follows:

$$\mathcal{G}(\mathbf{u}_{k,t}[\Omega]) = \mathbf{u}_{k+t,t}[\Omega]. \quad (2)$$

We assume that the neural operator \mathcal{G} is trained under the supervision of the dataset $\mathbb{D}_{\text{train}} := \{\mathbf{u}_{0,Mt}^i[\Omega]\}_{i=1}^I$ ($M \in \mathbb{N}^+$), where $\mathbf{u}_{0,Mt}^i[\Omega]$ is the i -th PDE series defined in $\Omega \times [0, Mt]$ and governed by the parameter $\theta^i \in \Theta$. Existing methods typically assume that all \mathbf{u}^i in $\mathbb{D}_{\text{train}}$ share the same θ [22; 25], or have known different parameters θ^i [1; 47]. However, we consider a more challenging scenario where data are generated from various physical systems (with varying but unknown θ^i in $\mathbb{D}_{\text{train}}$ and \mathbb{D}_{test}) and no additional knowledge of θ^i is provided during the training and test stages.

2.3 Forecasting stage of PIANO

As shown in Fig. 1.a, given the initial PDE fields $\mathbf{u}_{0,t}^i[\Omega]$, the forecasting stage of PIANO includes three steps: 1). **Infer** the PI embedding \mathbf{h}^i via the PI encoder \mathcal{P} ; 2). **Integrate** \mathbf{h}^i into neural operator \mathcal{G} to obtain a personalized operator \mathcal{G}^i for \mathbf{u}^i ; 3). **Predict** the subsequent PDE fields with the personalized operator \mathcal{G}^i . As a result, two key technical problems arise when performing the above plans. On the one hand, we need to decipher the PI information behind the PDE system without the supervision of known labels. To this end, we utilize contrastive learning to pre-train the PI encoder in a self-supervised manner and propose the physics-aware cropping strategy to constrain the learned representation to align with the physical prior. On the other hand, we need to integrate the PI embedding into the neural operator to obtain the personalized operator. In this paper, we borrow the technique from DyConv [6] and propose the split-merge trick to use the PI embedding fully.

2.4 Contrastive training stage of PI encoder

In this section, we introduce how to train an encoder \mathcal{P} for extracting the PI information from the training set $\mathbb{D}_{\text{train}} = \{\mathbf{u}_{0,Mt}^i[\Omega]\}_{i=1}^I$ which is generated from various PDE fields without the supervision of $\{\theta^i\}_{i=1}^I$. We begin by considering the scenario where θ^i is a spatiotemporal invariant, i.e., $\mathbf{u}_{k_1,t}^i[\Omega_1]$ and $\mathbf{u}_{k_2,t}^i[\Omega_2]$ share the same θ^i for all $k_1, k_2 \in [0, T]$ and $\Omega_1, \Omega_2 \subset \Omega$. When $\theta \in \Theta$ is identifiable, there exists a mapping \mathcal{M} satisfying the following property:

$$\mathcal{M}(\mathbf{u}_{k_1,t}^i[\Omega_1]) = \mathcal{M}(\mathbf{u}_{k_2,t}^i[\Omega_2]) = \theta^i. \quad (3)$$

However, the mapping \mathcal{M} that can directly output θ^i is not available due to the absence of θ . To decipher the information implying θ^i , we adopt the technique from SimCLR [4] to train \mathcal{P} in a self-supervised manner. In each mini-batch, we sample training data $\{\mathbf{u}_{0,Mt}^i[\Omega]\}_{i \in \mathcal{A}}$ from $\mathbb{D}_{\text{train}}$ with index set \mathcal{A} and randomly intercept two patches from each PDE sample, i.e., $\{\mathbf{u}_{k_1,t}^i[\Omega_1]\}_{i \in \mathcal{A}}$ and $\{\mathbf{u}_{k_2,t}^i[\Omega_2]\}_{i \in \mathcal{A}}$. The PI encoder \mathcal{P} maps each patch to a representation vector, denoted as $\mathbf{h}_i^v := \mathcal{P}(\mathbf{u}_{k_v,t}^i[\Omega_v])$ for $v \in \{1, 2\}$. Subsequently, we employ a two-layer MLP g as a projection head to obtain $\mathbf{z}_i^v = g(\mathbf{h}_i^v)$ (Fig. 1.b.i). Considering the PDE patches cropped from the same/different PDE series as positive/negative samples, the SimCLR loss can be expressed as follows:

$$\begin{aligned} \mathcal{L}_{\text{SimCLR}} = & -\frac{1}{2|\mathcal{A}|} \cdot \\ & \sum_{i \in \mathcal{A}} \left[\log \frac{\exp(\text{sim}(\mathbf{z}_1^i, \mathbf{z}_2^i)/\tau)}{\sum_{j \neq i} \sum_{v \in \{1,2\}} \exp(\text{sim}(\mathbf{z}_1^i, \mathbf{z}_v^j)/\tau)} + \right. \\ & \left. \log \frac{\exp(\text{sim}(\mathbf{z}_1^i, \mathbf{z}_2^i)/\tau)}{\sum_{j \neq i} \sum_{v \in \{1,2\}} \exp(\text{sim}(\mathbf{z}_2^i, \mathbf{z}_v^j)/\tau)} \right], \end{aligned} \quad (4)$$

where $\text{sim}(\mathbf{u}, \mathbf{v}) := \mathbf{u}^\top \mathbf{v} / \|\mathbf{u}\| \|\mathbf{v}\|$ denotes the cosine similarity between \mathbf{u} and \mathbf{v} , and $\tau > 0$ denotes a temperature parameter. As shown in Fig. 1.b.ii, the SimCLR loss brings closer the representations governed by the same physical parameters while pushing apart those with different parameters. After the training stage of contrastive learning, we throw away the projector g and only utilize the encoder \mathcal{P} to extract PI information from PDE fields, which is in line with the SimCLR method [4]. See Section **METHOD** for more details on the architecture of the PI encoder and the physics-aware cropping strategy.

2.5 Integrate the PI representation

In this section, we introduce how PIANO integrates the pre-trained PI representation into the neural operator. Given the pre-trained PI encoder \mathcal{P} and an initial PDE field $\mathbf{u}_{0,t}^i[\Omega]$, we first obtain the PI embedding \mathbf{h}^i via a split-merge trick (see Section **METHOD** for more details), and then we adopt the DyConv [6] technique to incorporate the PI information into the neural operator \mathcal{G} . In the first layer of \mathcal{G} , there are K convolutional matrices with the same size, denoted as $\{\mathbf{W}_{1,k}\}_{k=1}^K$. In detail, we transform the first Fourier/convolutional layer into a DyConv layer in the Fourier-based and convolutional-based neural operators, respectively. All other layers maintain the same structure as the original neural operators. When predicting the PDE fields for a specific instance \mathbf{u}^i , we use an MLP to transform its PI representation \mathbf{h}^i into K non-negative scales $\{a_k^i\}_{k=1}^K$, with $\sum_k a_k^i = 1$. The normalization of a_k^i is implemented by a softmax layer. We use $\{a_k^i\}_{k=1}^K$ as attention to reweight the K convolution matrices, i.e., $\mathbf{W}_1^i = \sum_k a_k^i \mathbf{W}_{1,k}$. We replace the first layer of \mathcal{G} with \mathbf{W}_1^i and denote this new operator as \mathcal{G}^i , which can be considered as the personalized operator for \mathbf{u}^i (Fig. 1.c). It is worth mentioning that the parameters \mathbf{W}_1^i in \mathcal{G}^i are obtained by the weighted summation, whose computational cost is almost negligible compared with the convolutional operation. Therefore, when aligning the parameters of PIANO and other neural operators, PIANO enjoys a comparable or faster inference speed, even considering the calculation of the PI representation \mathbf{h} .

3 EXPERIMENTS

In this section, we conduct a series of numerical experiments to assess the performance of our proposed PIANO method and other baseline techniques in simulating PDE systems governed by diverse PIs.

3.1 Experimental setup

We divide the temporal intervals into 200 frames for training and validation. The input and output frames are set as 20 for neural operator and PI encoders in the experiments. In order to assess the out-of-distribution generalization capabilities of the trained operator, we set the test temporal intervals at 240, with the last 40 frames occurring exclusively in the test set. We denote the temporal interval in the training set as the training domain, and the one that only occurs in the test set as the future domain. The spatial intervals are partitioned into 64 frames for the 1D case and 64×64 frames for the 2D case, respectively. The training, test and validation set sizes for all tasks are 1,000, 200, and 200, respectively. All experiments are carried out using the PyTorch package [30] on an NVIDIA A100 GPU. We repeat each experiment with three random seeds from the set $\{0, 1, 2\}$ and report the mean value and variance. The performance of the model is evaluated using the average relative ℓ_2 error (E_{ℓ_2}) and the ℓ_∞ error (E_{ℓ_∞}) over all frames in the training domain and the future domain, respectively.

3.2 Dataset

In this section, we introduce the PDE dataset utilized in this paper, including two kinds of Burgers' equation, the 1D CDE, and three kinds of 2D NSEs.

E1 (Burgers' equation with varying external forces f) We simulate the 1D Burgers' equation with varying external forces f , defined as follows:

$$\begin{aligned} \frac{\partial u}{\partial t} &= -u \frac{\partial u}{\partial x} + 0.1 \Delta u + 0.1 f(x), \quad x \in [-\pi, \pi], \\ u(\pm\pi, t) &= 0, \end{aligned} \quad (5)$$

where $f(x)$ is a smooth function representing the external force. In this experiment, we select fourteen different f to evaluate the performance of PIANO and other baseline methods under varying external forces. These forces are uniformly sampled from the set $\{0, 1, \cos(x), \cos(2x), \cos(3x), \sin(x), \sin(2x), \sin(3x), \pm \tanh(x), \pm \tanh(2x), \pm \tanh(3x)\}$. The ground-truth data are generated using the Python package 'py-pde' [51], with a fixed step size of 10^{-4} . The final time T is set to 5 for the training set and 6 for the test set, respectively.

E2 (Burgers' equation with varying diffusivities D) We simulate the 1D Burgers' equation with spatially varying diffusivities, defined as follows:

$$\begin{aligned} \frac{\partial u}{\partial t} &= -u \frac{\partial u}{\partial x} + 0.1 \nabla(D(x)) \cdot \nabla u, \quad x \in [-\pi, \pi], \\ u(\pm\pi, t) &= 0, \end{aligned} \quad (6)$$

where $D(x)$ is a smooth and non-negative function representing the spatially varying diffusivity. In this experiment, we select ten different diffusivities to evaluate the performance of PIANO and other baseline methods under varying spatial fields. Ten types of diffusivities are uniformly sampled from the set $\{1, 2, 1 \pm \cos(x), 1 \pm \sin(x), 1 \pm \cos(2x), 1 \pm \sin(2x)\}$. The data generation scheme and the final time T are aligned with the experiment E1.

E3 (CDE with varying boundary conditions \mathcal{B}) We simulate the 1D CDEs with varying boundary conditions, defined as follows:

$$\begin{aligned} \frac{\partial u}{\partial t} &= 0.1 \Delta u + 0.1 u + 0.1 \sin(2\pi x), \quad x \in [0, 1], \\ \mathcal{B}[u](x, t) &= 0. \end{aligned} \quad (7)$$

where $\mathcal{B}[u](x, t) = 0$ represents the boundary conditions. In this experiment, we select four types of \mathcal{B} to evaluate the generalizability of PIANO and other baseline methods under varying boundary conditions. In this dataset, four types of boundary conditions include the Dirichlet condition ($u = 0.2$), the Neumann condition ($\partial_n u = 0.2$), the curvature condition ($\partial_n^2 u = 0.2$), and the Robin condition ($\partial_n u + u = 0.2$). The data generation scheme and the final time T align with the experiment E1.

E4 (NSE with varying viscosity terms ν) We simulate the vorticity fields for 2D flows within a periodic domain $\Omega = [0, 1] \times [0, 1]$, governed by the following NSEs:

$$\begin{aligned}\frac{\partial \omega}{\partial t} &= -(\mathbf{u} \cdot \nabla)\omega + \nu \Delta \omega + f(\mathbf{x}), \\ \omega &= \nabla \times \mathbf{u},\end{aligned}\tag{8}$$

where $f(\mathbf{x}) = 0.1 \sin(2\pi(\mathbf{x}_1 + \mathbf{x}_2)) + 0.1 \cos(2\pi(\mathbf{x}_1 + \mathbf{x}_2))$ and $\nu \in \mathbb{R}^+$ represents the forcing function and viscosity term, respectively. The viscosity is a crucial component in NSEs that determines the turbulence of flows [41; 42]. We generate NSE data with varying viscosity coefficients to simulate heterogeneity, ranging from 10^{-2} to 10^{-5} . The viscosity fields become more complicated as the ν decreases because the nonlinear term $-(\mathbf{u} \cdot \nabla)\omega$ gradually governs the motion of the fluids. The data generation process employs the Pseudo-Spectral Method (PSM) with a time-step of 10^{-4} and a 256×256 grid size. The data are then downsampled to a grid size 64×64 , which aligns with the settings in [22]. The final time T is 20 and 24 for the train and the test set, respectively.

E5 (NSE with varying viscosity terms ν and external forces f) In this experiment, we aim to simulate the 2D NSE as shown in Eq. 8, with varying viscosity terms ν and external forces f . The viscosity coefficients ν range from 10^{-2} to 10^{-5} . The form of the forcing function is given by $f(\mathbf{x}) = a \sin(2\pi(\mathbf{x}_1 + \mathbf{x}_2)) + a \cos(2\pi(\mathbf{x}_1 + \mathbf{x}_2))$, where the coefficient a is uniformly sampled from $[0, 0.2]$. All other experimental settings are consistent with those described in E4.

E6 (Kolmogorov flow with varying viscosity terms ν) We simulate the vorticity fields for 2D NSEs within a periodic domain $\Omega = [0, 1] \times [0, 1]$ driven by the Kolmogorov forcing as follows [40]:

$$\begin{aligned}\frac{\partial \omega}{\partial t} &= -(\mathbf{u} \cdot \nabla)\omega + \nu \Delta \omega + 0.1 \cos(8\pi \mathbf{x}_1), \\ \omega &= \nabla \times \mathbf{u}.\end{aligned}\tag{9}$$

The fluid fields in Eq. 9 would result in much more complex trajectories due to the involvement of Kolmogorov forcing. We generate NSE data with varying viscosity coefficients to simulate heterogeneity, ranging from 10^{-2} to 10^{-4} . All other experimental settings are consistent with those described in E4.

3.3 Baselines

We consider several representative baselines from operator learning models, including:

- Fourier Neural Operator (FNO) [22]: A classical neural operator that uses the Fourier transform to handle PDE information in the frequency domain.
- Unet [36; 44]: A classic architecture for semantic segmentation in biomedical imaging, recently utilized as a surrogate model for PDE solvers.
- Low-rank decomposition Network (LordNet) [16]: A convolutional-based neural PDE solver that learns a low-rank decomposition layer to extract dominant patterns.
- MultiWavelet-based model (MWT) [12]: A neural operator that compresses the kernel of the corresponding operator using a fine-grained wavelet transform.
- Factorized Fourier Neural Operators (FFNO) [45]: A FNO variant that improves performance using a separable spectral layer and enhanced residual connections.

For PIANO, we conduct experiments on PIANO + X, where X represents the backbone models. For the neural operator X and PIANO + X, we align the critical parameters of X and adjust the widths of the networks to match the number of parameters between X and PIANO + X, thereby ensuring a fair comparison.

Table 2: **Results on PDE simulation for E1, E2, E3, E4, E5 and E6.** Relative errors (%) and computational costs for baseline methods and PIANO. The computational cost and numbers of parameters for PIANO reported in this table consider both the expenses of the PI encoder and neural operator. The best results in each task are in **bold**.

Data	Model	Training Domain		Future Domain		Time		Param
		E_{ℓ_2} (%)	E_{ℓ_∞} (%)	E_{ℓ_2} (%)	E_{ℓ_∞} (%)	Train (S)	Infer (S)	# (M)
E1 (Burgers' with varying external forces f)	FNO	0.669±0.124	0.978±0.029	1.062±0.039	1.340±0.158	0.128	0.018	0.757
	LordNet	1.660±0.058	2.406±0.262	2.782±0.111	3.529±0.213	0.317	0.138	0.810
	MWT	1.962±0.250	2.737±0.450	2.764±0.379	3.572±0.514	0.460	0.111	0.789
	Unet	2.576±0.124	4.205±0.108	3.280±0.084	4.687±0.158	0.256	0.041	0.860
	PIANO + FNO	0.492±0.045	0.611±0.045	0.536±0.046	0.700±0.038	0.147	0.022	0.762
	PIANO + Unet	1.605±0.264	3.130±0.685	1.796±0.386	2.946±0.526	0.299	0.039	0.766
E2 (Burgers' with varying diffusivities D)	FNO	6.328±0.162	10.847±0.251	13.111±0.384	19.379±0.649	0.128	0.018	0.757
	LordNet	8.471±0.628	22.016±6.849	23.786±7.989	62.977±35.304	0.317	0.138	0.810
	MWT	6.381±0.069	12.355±0.580	12.013±0.266	18.952±1.082	0.460	0.111	0.789
	Unet	7.087±1.680	12.592±2.750	13.593±3.413	20.221±5.280	0.256	0.041	0.860
	PIANO + FNO	4.559±0.092	8.932±0.312	8.421±0.440	13.680±1.174	0.147	0.022	0.762
	PIANO + Unet	4.149±0.985	8.879±1.106	7.342±2.072	12.330±3.015	0.299	0.039	0.766
E3 (CDE with varying boundary conditions β)	FNO	1.127±0.256	1.742±0.346	1.468±0.394	2.041±0.420	0.128	0.018	0.757
	LordNet	0.605±0.039	0.990±0.048	0.901±0.072	0.832±0.063	0.317	0.138	0.810
	MWT	0.662±0.037	1.232±0.107	0.781±0.113	1.385±0.148	0.460	0.111	0.789
	Unet	12.565±1.752	20.786±2.976	20.335±3.100	22.686±3.511	0.256	0.041	0.860
	PIANO + FNO	0.416±0.180	0.893±0.338	0.708±0.403	1.098±0.547	0.148	0.022	0.763
	PIANO + Unet	2.921±0.363	5.773±0.767	3.611±0.830	5.446±0.676	0.299	0.039	0.767
E4 (NSE with varying viscosity terms ν)	FNO	10.433±0.298	16.937±0.302	30.702±1.043	56.563±0.949	0.384	0.182	2.085
	LordNet	8.469±0.633	15.574±0.863	30.348±0.838	57.728±1.514	1.031	0.547	2.069
	MWT	10.135±0.346	17.917±0.253	32.232±0.713	61.572±1.487	1.067	0.229	2.295
	Unet	9.054±0.204	18.483±0.381	31.830±0.496	60.106±0.299	0.335	0.089	3.038
	FFNO	3.698±0.160	6.943±0.214	15.845±0.572	35.766±1.069	1.964	1.008	2.013
	PIANO + FNO	4.652±0.396	9.191±0.605	17.393±0.672	39.953±1.107	0.395	0.138	2.020
E5 (NSE with varying viscosity terms ν and external forces f)	PIANO + Unet	6.070±0.397	15.356±0.914	20.132±1.288	47.079±2.144	0.440	0.111	1.941
	PIANO + FFNO	3.140±0.100	5.935±0.098	12.155±0.237	28.985±0.456	1.364	0.682	1.888
	FNO	19.277±0.762	26.354±0.848	44.467±2.005	57.912±1.934	0.384	0.182	2.085
	LordNet	27.675±4.095	39.617±7.149	76.273±19.280	111.628±17.546	1.031	0.547	2.069
	MWT	18.908±0.768	25.361±0.764	40.919±1.317	53.123±1.087	1.067	0.229	2.295
	Unet	25.374±0.321	37.916±0.260	52.505±4.859	73.183±6.822	0.335	0.089	3.038
E6 (Kolmogorov flow with varying viscosity terms ν)	FFNO	8.032±0.575	11.607±0.781	20.750±1.188	28.939±1.652	1.964	1.008	2.013
	PIANO + FNO	9.082±0.238	12.731±0.525	21.795±0.833	29.912±1.176	0.457	0.144	2.071
	PIANO + Unet	12.829±0.440	23.184±1.812	24.060±1.081	40.415±1.803	0.491	0.115	2.158
	PIANO + FFNO	6.937±0.199	9.736±0.215	18.062±0.913	25.411±0.920	1.424	0.686	1.997
	FNO	4.017±0.101	5.250±0.171	5.241±0.027	6.842±0.219	0.384	0.182	2.085
	LordNet	6.559±0.969	8.159±2.259	11.343±1.448	17.940±8.683	1.031	0.547	2.069
E6 (Kolmogorov flow with varying viscosity terms ν)	MWT	4.663±0.285	5.769±0.350	6.511±0.103	8.062±0.272	1.067	0.229	2.295
	Unet	9.807±2.673	19.449±6.144	13.949±3.593	27.505±9.510	0.335	0.089	3.038
	FFNO	1.727±0.050	2.194±0.052	2.608±0.067	3.357±0.050	1.964	1.008	2.013
	PIANO + FNO	1.908±0.074	2.419±0.040	2.840±0.126	3.552±0.126	0.395	0.138	2.020
	PIANO + Unet	6.704±0.201	12.143±0.119	9.676±0.248	16.495±0.168	0.440	0.111	1.941
	PIANO + FFNO	1.491±0.037	1.876±0.023	2.277±0.110	3.040±0.155	1.364	0.682	1.888

3.4 Results

Table 2 presents the performance of various models for the PDE simulation on the experiments (E1-E6), as well as their computational costs. PIANO achieves the best prediction results across most metrics and experiments. When compared with the backbone models X (FNO, Unet, and FFNO), the three variants of PIANO + X consistently outperform their backbone models on all tasks for both E_{ℓ_2} and E_{ℓ_∞} errors, demonstrating that the PI embedding can enhance the robustness and accuracy of neural operators' prediction capabilities. Specifically, PIANO + FNO, compared to FNO, reduces the error rate E_{ℓ_2} by 26.5%-63.1% in the training domain and by 35.7%-51.7% in the future domain over four experiments, respectively. PIANO + Unet, compared to Unet, reduces the error rate E_{ℓ_2} by 32.9%-76.8% in the training domain and by 36.7%-82.2% in the future domain over four experiments, respectively. PIANO provides a more significant enhancement to Unet than FNO in most tasks. One potential explanation is that the Fourier layer within the PI encoder introduces additional frequency domain information to the convolution-based Unet. In contrast, FNO is already based on a Fourier layer network. We compare the vorticity fields (in E4 and E6) predicted by FNO and PIANO + FNO from $T = 4$ to $T = 24$ in Fig. 2. Within the training domain, PIANO demonstrates a superior ability to capture the intricate details of fluid dynamics compared to FNO. As for the future domain, where supervised data are lacking, PIANO and FNO struggle to provide exact predictions in E4. However, PIANO still forecasts the corresponding

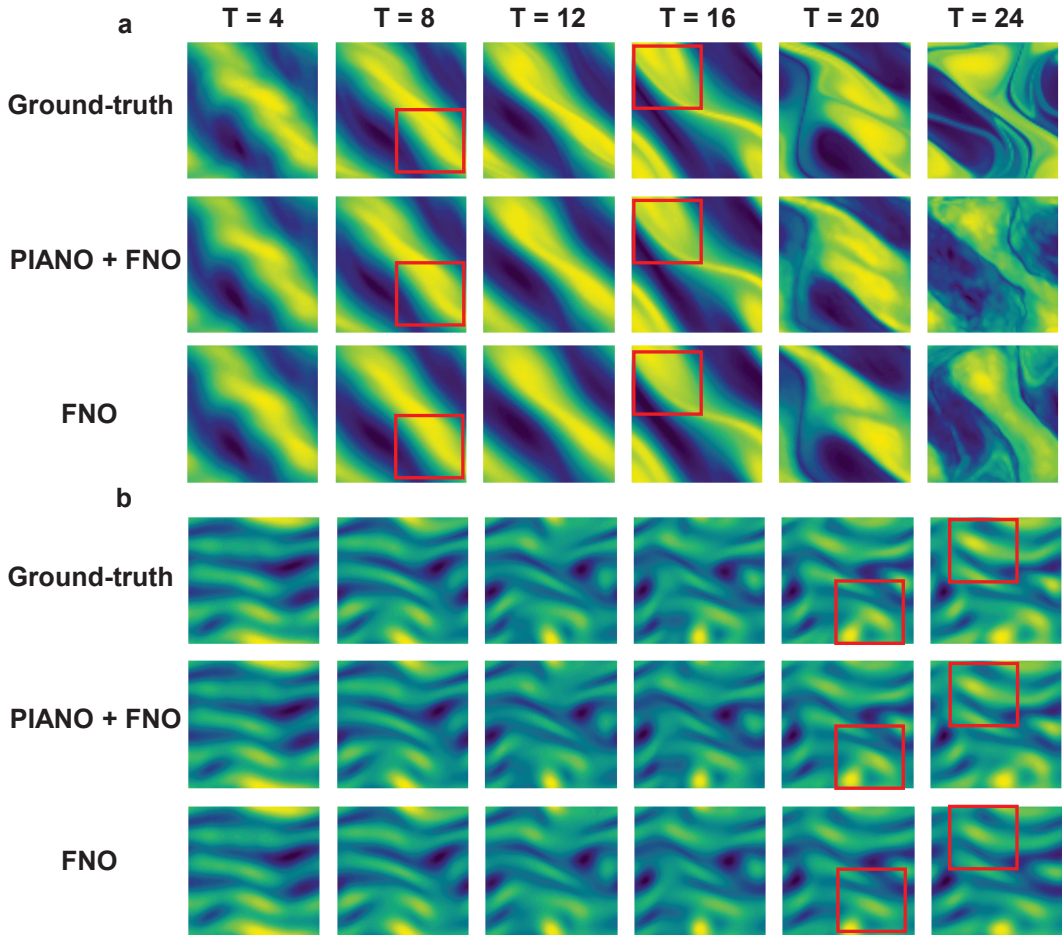


Figure 2: **Comparison of the vorticity fields in E4 (a) and E6 (b) between the FNO and PIANO + FNO from $T = 4$ to 24 in the periodic domain $[0, 1]^2$ for a 2D turbulent flow.** Please note the time $T = \{4, 8, 12, 16, 20\}$ are in the training domain, while $T = 24$ is in the future domain. The vorticity fields in the red boxes indicate that PIANO can capture more details than FNO.

trends of fluids more accurately than FNO.

Regarding computational costs, it is worth mentioning that the PI encoder is a significantly lighter network (0.053 M and 0.184 M for Burgers' and NSE cases) compared to the neural operator. As a result, the inference time added by the PI encoder is generally negligible, which is 0.002S and 0.004S for Burgers' and NSE data, respectively. Furthermore, in situations where the computational cost of the convolutional layers in the backbone is substantial, PIANO can considerably enhance the computation speed with the help of dynamic convolutional techniques. For example, PIANO can reduce the inference time by 24.2% and 32.3% for FNO and FFNO, respectively, when simulating 2D NSEs. More detailed discussions on computational costs can be seen in the supplementary material.

3.5 Physical Explanation of PI encoder

In this section, we conduct experiments to investigate the physical significance of the PI encoder on Burgers' (E1) and NSE (E4) data, specifically, whether the learned representation can reflect the PI information hidden within the PDE system. We consider two kinds of downstream tasks, including unsupervised dimensionality reduction and supervised classification (regression), to analyze the properties of PI embeddings for PIANO. Furthermore, we compare several corresponding baselines to study the effects of each component in PIANO as follows:

- **PIANO-CL**: In this model, we jointly train the PI encoder and neural operator without the contrastive pre-training, which can be regarded as an FNO version for DyConv. We train this model to reveal

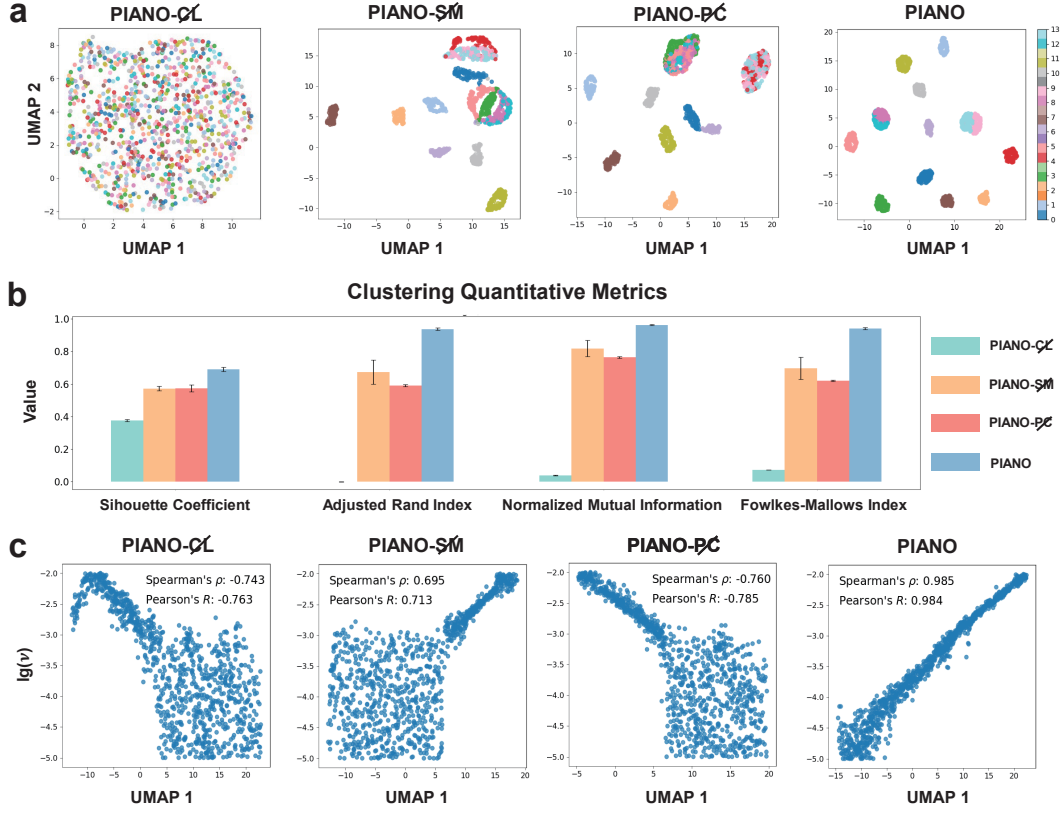


Figure 3: The performances of learned representation on the unsupervised dimensionality reduction tasks. CL, SM, and PC are the abbreviations of contrastive learning, the split-merge trick, and the physics-aware cropping strategy, respectively. **a**: The dimensionality reduction results of PI embeddings via UMAP for Burgers' data. The horizontal and vertical axes represent the two main components of UMAP, and each color represents a different external force in the dataset. Colors numbered from 0 to 13 correspond to the fourteen types of external forces, including $0, 1, \cos(x), \sin(x), -\tanh(x), \tanh(x), \cos(2x), \sin(2x), \tanh(2x), -\tanh(2x), \cos(3x), \sin(3x), \tanh(3x),$ and $-\tanh(3x)$. **b**: Four metrics to evaluate the quantity of clustering via representation vectors given by different methods, including Silhouette Coefficient, Adjusted Rand Index, Normalized Mutual Information, and Fowlkes-Mallows Index. All four of these metrics indicate that the larger the value, the better the clustering performance. **c**: The dimensionality reduction results of the PI embeddings via UMAP for the NSE data. The horizontal axis and the vertical axis represent the first component of UMAP and the logarithmic viscosity term $\lg(\nu)$ in the dataset. We also calculate the Spearman and Pearson correlation coefficients between the first component and logarithmic viscosity term $\lg(\nu)$, which represent the rank order and linear relationships between two variables, respectively.

the impact of contrastive learning in PIANO.

- PIANO-SM: In PIANO, we utilize the split-merge trick to divide the PDE fields Ω into several patches $\{\Omega_v\}_{v=1}^V$ and then input them into the PI encoder during the training and testing phases (Fig. 1.(b, c)). In PIANO-SM, we directly feed the entire PDE fields into the PI encoder.
- PIANO-PC: We assert that cropping strategies should align with the physics prior of the PDE system and propose physics-aware cropping methods for contrastive learning (Fig. 1.b). In PIANO-PC, we discard the physics-aware cropping technique and swap two corresponding augmentation methods for Burgers' and NSE data, respectively.

For dimensionality reduction tasks, we utilize UMAP [27] to project the PI embedding into a 2D and 1D manifold for Burgers' and NSE data, respectively (Fig. 3). For Burgers' data, PIANO-CL fails to obtain a meaningful representation, highlighting the importance of contrastive learning. PIANO-SM and PIANO-PC can distinguish half of the external force types but struggle to separate some similar

Table 3: **The performances of learned representation on the supervised tasks.** Accuracy (relative ℓ_2 error) of the PI encoder in PIANO and other baselines using linear evaluation on Burgers’ equation (NSE). CL, SM, and PC are the abbreviations of contrastive learning, split-merge trick, and physics-aware cropping strategy, respectively. The best results in each task are in **bold**.

Method	Burgers’ (Acc., \uparrow)	NSE (ℓ_2 Error, \downarrow)
PIANO- CL	0.078 \pm 0.003	0.161 \pm 0.034
PIANO- SM	0.988 \pm 0.008	0.086 \pm 0.011
PIANO- PC	0.955 \pm 0.013	0.092 \pm 0.004
PIANO	0.997\pm 0.003	0.033\pm 0.002

functions, such as $-\tanh(kx)$ for $k \in \{1, 2, 3\}$. Only PIANO achieves remarkable clustering results (Fig. 3.a). We also calculate four clustering metrics to quantitatively evaluate the performance of clustering (Fig. 3.b), where the clustering results are obtained via K-Means [14] with the PI representation. These four metrics include Silhouette Coefficient, Adjusted Rand Index, Normalized Mutual Information, and Fowlkes-Mallows Index, which assess the clustering quality through measuring intra-cluster similarity, agreement between partitions, shared information between partitions, and the similarity of pairs within clusters, respectively. The larger their values, the better the clustering quality. As shown in Fig. 3.b, PIANO is the only method that achieves a Silhouette Coefficient greater than 0.65 and values larger than 0.90 for the other three metrics, significantly outperforming the other methods. For NSE data, PIANO is the only method where the first component of PI embeddings exhibits a strong correlation with the logarithmic viscosity term (with correlation coefficients greater than 98%). At the same time, the other three PIANO variants fail to distinguish viscosity terms ranging from 10^{-3} to 10^{-5} (Fig. 3.b).

For supervised tasks, we train a linear predictor \mathcal{T} that maps the learned representation \mathbf{h}^i to the corresponding PDE parameters θ^i under the supervision of ground-truth labels (Table 3). For the dataset of Burgers’ equation, which involves fourteen types of external forces, the training of \mathcal{T} naturally becomes a softmax regression problem. In the case of NSE, where the viscosity term continuously changes, we treat the training of \mathcal{T} as a ridge regression problem. According to the supervised downstream tasks, the PI encoder trained in PIANO exhibits the best ability to predict the PIs in Burgers’ equation and NSE compared to other baseline methods, which aligns with the experimental result in the unsupervised part.

The results of downstream tasks indicate that PIANO can represent the physical knowledge via a low-dimensional manifold and predict corresponding PDE parameters, thus demonstrating the physical meaning of PIANO.

4 CONCLUSION

In this paper, we introduce PIANO, an innovative operator learning framework designed to decipher the PIs information from PDE series with various physical mechanisms and integrate them into neural operators to conduct forecasting tasks. We propose the physics-aware cropping technique to enhance consistency with physical priors and the split-merge trick to fully utilize the physical information across the spatial domain. According to our numerical results, PIANO successfully overcomes the limitations of current neural operator learning methods, thereby demonstrating its capability to process PDE data from a diverse range of sources and scenarios. Furthermore, the results of a series of downstream tasks verify the physical significance of the extracted PI representation by PIANO.

We propose the following future works to enhance the capabilities and applications of PIANO further:

- Expanding PIANO to PDE types with varying geometries: In this study, we primarily focused on 1D equations when simulating PDEs with varying boundary conditions. However, it would be valuable to explore the extension of PIANO to more complex PDEs, such as PDEs with 2D and 3D complex geometries.
- Addressing large-scale challenges using PIANO: In large-scale real-world problems, such as weather forecasting, PIANO can potentially extract meaningful PI representations, such as geographical information of various regions. This capability could enhance the accuracy and reliability of forecasting tasks and other large-scale applications.

- Integrating additional physical priors into PIANO: Our current study assumes that the underlying PI in the PDE system is time-invariant. However, real-world systems often exhibit other physical properties, such as periodicity and spatial invariance. By incorporating these additional physical priors into the contrastive learning stage, PIANO could be applied to a broader range of problems.

5 METHOD

5.1 The architecture of PI encoder

In this paper, the architecture of \mathcal{P} consists of six layers, successively including two Fourier layers [22], two convolutional layers, and two fully connected layers. The Fourier layers can extract the PDE information in the frequency space, and other layers downsample the feature map to a low-dimensional vector. We employ the ‘GeLU’ function as the activation function. It is important to note that we only feed a sub-patch of the PDE field to \mathcal{P} , and the output of \mathcal{P} is a low-dimensional vector. Furthermore, the amount of information required to infer PIs is significantly less than that needed to forecast the physical fields in a PDE system. Consequently, compared with the main branch of the neural operator, this component is a lightweight network that can extract PIs and enjoys fast inference speed.

5.2 Physics-aware cropping strategy

The cropping of the PDE series can be interpreted as data augmentation in contrastive learning. Unlike previous argumentation methods in vision tasks [9; 29; 31; 49], the ones for PDEs representation should comply with the physical prior accordingly. We have previously discussed cases where the PI represents spatiotemporal invariants. When the PI is only a temporal invariant and exhibits spatial variation, such as an external force, it is necessary to align spatial positions when implementing the crop operator. As a result, we extract two patches from the same spatial location for each PDE sample, i.e., $\{\mathbf{u}_{k_1,t}^i[\Omega^i]\}_{i \in \mathcal{A}}$ and $\{\mathbf{u}_{k_2,t}^i[\Omega^i]\}_{i \in \mathcal{A}}$. For boundary invariants, we need to crop the PDE patches near the boundary to encode the boundary conditions. We illustrate all three cropping methods in Fig. 1.b.iii. Note that we also illustrate another cropping approach, called the global cropping technique, which directly selects the PDE patch across the entire spatial field as augmentation samples, i.e., $\{\mathbf{u}_{k_1,t}^i[\Omega]\}_{i \in \mathcal{A}}$ and $\{\mathbf{u}_{k_2,t}^i[\Omega]\}_{i \in \mathcal{A}}$. This global cropping strategy considers the time-invariant property of PIs while ignoring the more detailed physical priors of different types of PIs.

5.3 Split-merge trick

We split the PDE fields according to the physical prior in the contrastive training stage. Compared to global cropping, such a splitting strategy can encode the physical knowledge into \mathcal{P} through a more accurate approach. In the forecasting stage, we split the initial PDE fields $\mathbf{u}_{0,t}^i[\Omega]$ into V uniform and disjointed patches $\{\mathbf{u}_{0,t}^i[\Omega_v]\}_{v=1}^V$, which are aligned with the patch size in the pre-training stage and satisfy $\cup_v \Omega_v = \Omega$. We feed all patches into \mathcal{P} to obtain the corresponding representations $\mathbf{h}_v^i = \mathcal{P}(\mathbf{u}_{0,t}^i[\Omega_v])$, and merge them together as the PI vector of \mathbf{u}^i , i.e., $\mathbf{h}^i := [\mathbf{h}_1^i, \dots, \mathbf{h}_V^i]$ (Fig. 1.c). This merge operation can make full use of the PDE information. In practice, we fix the parameters of the pre-trained PI encoder \mathcal{P} and only optimize the neural operator \mathcal{G} in the training stage.

6 EXPERIMENTAL DETAILS

In this section, we introduce the experimental details in the main body.

6.1 Examples of the dataset

Examples of each dataset can be seen in Supplementary Fig. 4.

6.2 Baselines

We consider several representative baselines from operator learning models, including:

- Fourier Neural Operator (FNO) [22]: A classical neural operator that uses the Fourier transform to handle PDE information in the frequency domain. The number of layers for FNO is fixed at 4, and we set the `modes` of the Fourier layer at 16 and 12 for the 1D and 2D cases, respectively, which is selected from the set $\{12, 16, 20\}$.
- Unet [36; 44]: A classic architecture for semantic segmentation in biomedical imaging, recently utilized as a surrogate model for PDE solvers. The architecture of Unet is in line with the PDE benchmark paper [44], and we adjust the width of the convolutional layers to make its size align with other baselines.
- Low-rank decomposition Network (LordNet) [16]: A convolutional-based neural PDE solver that learns a low-rank decomposition layer to extract dominant patterns. The architecture of LordNet is in line with its original paper, and we adjust the width of the convolutional layers to make its size align with other baselines.
- MultiWavelet-based model (MWT) [12]: A neural operator that compresses the kernel of the corresponding operator using a fine-grained wavelet transform. The architecture of MWT is in line with its original paper, and we select the parameter α in the MultiWavelet layer from the set $\{16, 18, 20\}$.
- Factorized Fourier Neural Operators (FFNO) [45]: A FNO variant that improves performance using a separable spectral layer and enhanced residual connections. Since the codes for FFNO are only available for 2D cases, we only conduct it on 2D NSE data. The number of layers for FFNO is fixed at 6, and we fix the modes of the Fourier layer at 12 for 2D cases, respectively, which is selected from the set $\{12, 16, 20\}$.

For PIANO, we conduct experiments on PIANO + X, where X represents the backbone models. For the neural operator X and PIANO + X, we align the critical parameters of X (e.g., modes in FNO and FFNO, number of layers in neural networks) and adjust the widths of the networks to match the number of parameters between X and PIANO + X, thereby ensuring a fair comparison. These critical parameters in the baseline methods are chosen with the help of validation set. In 1D cases, we choose FNO and Unet as backbone models for PIANO and additionally incorporate FFNO for 2D cases. The PI encoder in PIANO is a much lighter network compared to its backbone model. For Burgers' data, the PI encoder is stacked with two Fourier layers (`modes` = 10, `width` = 10), two convolutional layers (`width` = 10, `kernel_size` = 4) and a two-layer MLP. For CDE data, the PI encoder is stacked with two Fourier layers (`modes` = 8, `width` = 16), two convolutional layers (`width` = 10, `kernel_size` = 4), and a two-layer MLP. For NSE, the PI encoder is stacked with two Fourier layers (`modes` = 10, `width` = 12), two convolutional layers (`width` = 12, `kernel_size` = 4) and a two-layer MLP. For the backbone model in PIANO, we modify its first layer to the DyConv layer and the number of DyConv layers K is fixed at 4 for all tasks.

6.3 Training details

For each method, we employ the AdamW optimizer [24] to train the neural network for 20,000 epochs, using an initial learning rate of `lr`. The learning rate is decayed by 0.8 every 5,000 epoch. The optimal initial learning rate `lr` is chosen from the set $\{0.001, 0.002, 0.005, 0.01\}$ for each method with the help of validation set. A fixed batch size of 200 is used throughout the training process. In the training stage, we evaluate the model's performance on the validation data every 20 epoch and apply early stopping to the optimization if the model's performance does not improve in 2,000 iterations. During the contrastive training stage in PIANO, we also use the AdamW optimizer [24] to train the neural network for 20,000 epochs, with an initial learning rate of `lr` = 0.001 and a learning rate decay factor of 0.5 every 4,000 epochs. Batch size and temperature parameter τ are maintained at 512 and 0.5, respectively. Please note that the PIs in E1-E6 correspond to different PIs, including spatiotemporal invariant, boundary invariant, and temporal invariant, respectively. Therefore, we need to utilize the corresponding cropping strategies. Moreover, we need to train two PI encoders for E5 and combine the corresponding PI embeddings because there are two types of invariants in the settings. When conducting the split-merge trick, we set the spatial resolution to 32 for 1D scenarios and 32×32 for 2D scenarios, respectively. In the SimCLR settings, the dimensions of h and z are set as 64 and 32, respectively.

Table 4: **Computational costs of PIANO and its corresponding backbone model.** The training of PIANO consists of two parts: the PI encoder (PE) and the neural operator (NO). During the inference stage, PIANO first encodes the initial field of the PDE into its corresponding PI embedding, and calculates the attention (ATT) to obtain a personalized neural operator (PNO). After that, PIANO predicts the subsequent PDE field using this personalized neural operator.

Data	Model	Training Time (s)			Inference Time (s)				Model Size (M)			
		PE	NO	Total	PE	ATT	NO	Total	PE	NO	Total	PNO
E1	FNO	–	0.128	0.128	–	–	0.018	0.018	–	–	0.757	–
	PIANO + FNO	0.029	0.118	0.147	0.002	0.004	0.016	0.022	0.053	0.709	0.762	0.553
E2	FNO	–	0.384	0.384	–	–	0.182	0.182	–	–	2.085	–
	PIANO + FNO	0.067	0.328	0.395	0.004	0.011	0.123	0.138	0.184	1.836	2.020	1.024
	FFNO	–	1.964	1.964	–	–	1.008	1.008	–	–	2.013	–
	PIANO + FFNO	0.067	1.297	1.364	0.004	0.010	0.668	0.682	0.184	1.704	1.888	1.136

6.4 Computational costs

We present the computational cost in the training and inference stages for PIANO and its corresponding backbone models in Supplementary Table 4. We summarize our observations as follows:

- The training costs for the PI encoder are relatively low compared to the training costs of the neural operator. The reason is that we use the split-merge trick to divide the physics fields into smaller patches (e.g., from 64×64 to 32×32 in E2), and the model size of the PI encoder is much lighter compared to the neural operator.
- During the inference stage, PIANO first encodes the initial field of the PDE into its corresponding PI embedding and calculates the attention to obtain a personalized neural operator. Given the small size of the PI encoder and the fact that attention in the DyConv only involves weighted summation calculations, these computations are lightweight. As we have aligned the model size of PIANO + X with X, the scale of the personalized neural operator is significantly smaller than that of the original operator X. Therefore, it can predict subsequent PDE fields faster once the personalized operator is determined.
- In the 1D case, due to the inherent speed of the neural operator, the inference speeds of PIANO and PIANO + X are similar. However, in 2D cases, inference speed is significantly different between neural operators of different scales. Therefore, the benefits brought by PIANO become more apparent.

7 ADDITIONAL ANALYSES FOR PI ENCODER

In this section, we conduct additional experiments to examine the effects and properties of the PI encoder in PIANO. First, we perform ablation studies to uncover the impact of specific technical aspects of the PI encoder. Next, we study the effects of two hyperparameters, including `batch_size` and the temperature τ in contrastive learning for PIANO. Finally, we investigate the out-of-distribution (OOD) generalization ability of the PI encoder and the its performance in the real-world scenario.

7.1 The ablation studies on PI encoder

In this section, we conduct ablation studies to demonstrate the effects of essential components within the PI encoder for PDE forecasting tasks on Burgers’ (E1) and NSE (E4) data. Revisiting the training stages of the PI encoder, contrastive learning plays an essential role in extracting the underlying PIs for PDE systems. Additionally, we utilize some technical tricks to enhance the performance of PI encoders, including the split-merge trick and the physics-aware cropping strategy. To evaluate the effects of each component in PIANO, we compare several corresponding baselines as follows:

- **PIANO-CL**: In this model, we jointly train the PI encoder and neural operator without the contrastive pre-training, which can be regarded as an FNO version for DyConv. We train this model to reveal the impact of contrastive learning in PIANO.

Table 5: **Results of ablation studies on Burgers’ and NSE data.** Relative ℓ_2 errors (E_{ℓ_2} , %) for baseline methods and PIANO on training and future domains. CL, SM, and PC are the abbreviations of contrastive learning, split-merge trick, and physics-aware cropping strategy, respectively. The best results in each task are in **bold**.

Data	Model	Training Domain	Future Domain
Burgers’	FNO	0.668 \pm 0.039	1.062 \pm 0.039
	PIANO- CL	0.782 \pm 0.010	1.253 \pm 0.030
	PIANO- SM	0.662 \pm 0.021	0.845 \pm 0.062
	PIANO- PC	0.691 \pm 0.046	0.884 \pm 0.080
	PIANO	0.492\pm 0.045	0.536\pm 0.046
NSE	FNO	10.433 \pm 0.298	30.702 \pm 1.043
	PIANO- CL	11.978 \pm 0.733	35.543 \pm 3.938
	PIANO- SM	5.566 \pm 0.328	22.196 \pm 1.148
	PIANO- PC	5.882 \pm 0.328	22.881 \pm 0.978
	PIANO	4.652\pm 0.396	17.393\pm 0.672

Table 6: **The effects of hyper-parameters on the quality of the PI representations in contrastive learning.** Accuracy (relative ℓ_2 error) of the PI encoder trained with varying `batch_size` and τ using linear evaluation on Burgers’ equation (NSE). The best results in each task are in **bold**.

The effects of <code>batch_size</code>				
<code>batch_size</code>	64	128	256	512
Burgers’ (Acc., \uparrow)	0.985 \pm 0.009	0.985 \pm 0.009	0.993 \pm 0.003	0.997\pm 0.003
NSE (ℓ_2 Error, \downarrow)	0.035 \pm 0.002	0.033 \pm 0.002	0.032\pm 0.001	0.033 \pm 0.002
The effects of τ				
τ	0.01	0.05	0.1	0.5
Burgers’ (Acc., \uparrow)	0.987 \pm 0.008	0.985 \pm 0.009	0.988 \pm 0.003	0.997\pm 0.003
NSE (ℓ_2 Error, \downarrow)	0.045 \pm 0.007	0.051 \pm 0.006	0.048 \pm 0.006	0.033\pm 0.002

- PIANO-~~SM~~: In PIANO, we utilize the split-merge trick to divide the PDE fields Ω into several patches $\{\Omega_v\}_{v=1}^V$ and then input them into the PI encoder during both training and testing phases. In PIANO-~~SM~~, we directly feed the entire PDE fields into the PI encoder, i.e., utilize the global cropping method.
- PIANO-~~PC~~: We assert that the cropping strategies should align with the physical prior of the PDE system and propose the physics-aware cropping methods for contrastive learning. In PIANO-~~PC~~, we discard the physics-aware cropping technique and swap two corresponding augmentation methods for Burgers’ and NSE data, respectively.

Based on the ablation experiment results for Burgers’ and NSE data (Supplementary Table 5), the performance of PIANO-~~CL~~ is even worse than that of the plain FNO, which highlights the crucial role of contrastive learning in PIANO. Moreover, two distinct variations of PIANO, namely PIANO-~~SM~~ and PIANO-~~PC~~, demonstrate inferior performance in comparison to the original PIANO model, which indicates that we need to consider the properties of PIs and make the most of them during the training stages of PI encoder.

7.2 The effects of hyper-parameters in contrastive training

According to the existing SimCLR experiences reported in [4], two hyperparameters, `batch_size` and the temperature τ , have a significant impact on the quality of the representations. In this section, we study the effects of these two hyperparameters on the quality of PI representations. Firstly, we fix the hyperparameter τ to 0.5 and train the PI encoders with the `batch_size` values from the set $\{64, 128, 256, 512\}$. Similarly, we fix the hyperparameter `batch_size` to 512 and train the PI encoders with the τ values of the

set $\{0.01, 0.05, 0.1, 0.5\}$. Supplementary Table 6 presents the effects of hyperparameters on the quality of PI representations in contrastive learning using linear evaluation. The performance of the PI encoder remains relatively stable with changes in `batch_size` for both Burgers' equation and NSE, particularly when `batch_size` is greater than 256. Regarding the temperature parameter τ , the performance of the PI encoder for both Burgers' equation and NSE generally improves as it increases, suggesting that a relatively larger τ is recommended for training the PI encoder with SimCLR in PIANO.

7.3 OOD generalization ability of PI encoder

In this section, we conduct experiments to evaluate the out-of-distribution (OOD) generalization ability of the PI encoders in PIANO on E1 and E4. In E1, we add two groups of PDE data driven by external forcing $\cos(4x)$ and $\sin(4x)$. In E2, we add fluid fields with viscosity terms ranging from $[10^{-2}, 10^{-1}]$. Please note that the PI corresponding to these newly added data has never appeared in the training set. We use UMAP to map the PI embeddings to a low-dimensional space and show the results in Supplementary Fig. 5. It is interesting to see that the PI encoder can distinguish PDE fields outside the distribution. However, according to our experiments, PIANO fails to obtain meaningful forecasting results on PDE simulation tasks on out-of-distribution data. For instance, the relative error in E1 on the OOD data is larger than 40%, while the one on in-distribution data is less than 0.5%. One potential reason is that forecasting is much more challenging than learning PI, so data may be indispensable. One promising direction is to leverage few-shot learning techniques to transfer PIANO to other distributions [?], which we leave as an important future work.

7.4 PI in the real-world scenario

In this section, we train the PI encoder on weather forecasting data [15] to demonstrate our assumptions and motivations in real-world scenarios. When training the PI encoder, we utilize the prior knowledge that geographical information such as altitude and coastline does not change over time. Therefore, we regard them as spatial invariants and use the corresponding cropping techniques in the contrastive learning stage.

In detail, we consider two kinds of weather data in this section, including the 2m temperature for the mainland (red box in Supplementary Fig. 6.a) and the sea surface temperature data (green box in Supplementary Fig. 6.a). The range of mainland data is from 15 degrees north latitude to 75 degrees north latitude, and from 60 degrees east longitude to 120 degrees east longitude. The range of sea data is from 60 degrees south latitude to the equator, and from 150 degrees west longitude to 90 degrees west longitude. The series in the dataset is randomly sampled from the temperature data of the full year from 2020 to 2022.

To demonstrate that the trained PI embedding indeed contains geographical information, we select six different regions from each dataset and cut 200 series corresponding to different times from each region. Each series has a spatial resolution of 64×64 , with each grid point representing the average temperature at a location of 0.25° longitude and 0.25° latitude. Each series has 168 frames, with an interval of two hours between each frame. We use UMAP to reduce the dimensionality of these 1200 series' PI embeddings to a 2D low-dimensional space for land and sea datasets, respectively. The dimensionality reduction results in Supplementary Fig. 6 indicate that the PI encoder can distinguish different geographical regions, i.e., it has learned the corresponding geographical information.

References

- [1] Johannes Brandstetter, Daniel E. Worrall, and Max Welling. Message passing neural PDE solvers. In *International Conference on Learning Representations*, 2022.
- [2] Shuhao Cao. Choose a transformer: Fourier or galerkin. In A. Beygelzimer, Y. Dauphin, P. Liang, and J. Wortman Vaughan, editors, *Advances in Neural Information Processing Systems*, 2021.
- [3] Jingrun Chen, Xurong Chi, Weinan E, and Zhouwang Yang. Bridging traditional and machine learning-based algorithms for solving pdes: The random feature method. *Journal of Machine Learning*, 1(3):268–298, 2022.

- [4] Ting Chen, Simon Kornblith, Mohammad Norouzi, and Geoffrey Hinton. A simple framework for contrastive learning of visual representations. In *International conference on machine learning*, pages 1597–1607, 2020.
- [5] Wenqian Chen, Qian Wang, Jan S Hesthaven, and Chuhua Zhang. Physics-informed machine learning for reduced-order modeling of nonlinear problems. *Journal of computational physics*, 446:110666, 2021.
- [6] Yinpeng Chen, Xiyang Dai, Mengchen Liu, Dongdong Chen, Lu Yuan, and Zicheng Liu. Dynamic convolution: Attention over convolution kernels. In *Proceedings of the IEEE/CVF conference on computer vision and pattern recognition*, pages 11030–11039, 2020.
- [7] Zhao Chen, Yang Liu, and Hao Sun. Physics-informed learning of governing equations from scarce data. *Nature communications*, 12(1):6136, 2021.
- [8] Diego Córdoba, Marco A Fontelos, Ana M Mancho, and Jose L Rodrigo. Evidence of singularities for a family of contour dynamics equations. *Proceedings of the National Academy of Sciences*, 102(17):5949–5952, 2005.
- [9] Michael Dorcenwald, Fanyi Xiao, Biagio Brattoli, Joseph Tighe, and Davide Modolo. Scvrl: Shuffled contrastive video representation learning. In *Proceedings of the IEEE/CVF Conference on Computer Vision and Pattern Recognition*, pages 4132–4141, 2022.
- [10] Stefania Fresca, Luca Dede’, and Andrea Manzoni. A comprehensive deep learning-based approach to reduced order modeling of nonlinear time-dependent parametrized pdes. *Journal of Scientific Computing*, 87:1–36, 2021.
- [11] Shiqi Gong, Peiyan Hu, Qi Meng, Yue Wang, Rongchan Zhu, Bingguang Chen, Zhiming Ma, Hao Ni, and Tie-Yan Liu. Deep latent regularity network for modeling stochastic partial differential equations. In *Proceedings of the AAAI Conference on Artificial Intelligence*, volume 37, pages 7740–7747, 2023.
- [12] Gaurav Gupta, Xiongye Xiao, and Paul Bogdan. Multiwavelet-based operator learning for differential equations. *Advances in neural information processing systems*, 34:24048–24062, 2021.
- [13] Jiequn Han, Arnulf Jentzen, and Weinan E. Solving high-dimensional partial differential equations using deep learning. *Proceedings of the National Academy of Sciences*, 115(34):8505–8510, 2018.
- [14] J. A. Hartigan and M. A. Wong. Algorithm as 136: A k-means clustering algorithm. *Journal of the Royal Statistical Society. Series C (Applied Statistics)*, 28(1):100–108, 1979.
- [15] Hans Hersbach, Bill Bell, Paul Berrisford, Gionata Biavati, András Horányi, Joaquín Muñoz Sabater, Julien Nicolas, Carole Peubey, Raluca Radu, Iryna Rozum, et al. Era5 hourly data on single levels from 1979 to present. *Copernicus climate change service (c3s) climate data store (cds)*, 10(10.24381), 2018.
- [16] Xinquan Huang, Wenlei Shi, Qi Meng, Yue Wang, Xiaotian Gao, Jia Zhang, and Tie-Yan Liu. NeuralStagger: Accelerating physics-constrained neural PDE solver with spatial-temporal decomposition. In *Proceedings of the 40th International Conference on Machine Learning*, volume 202, pages 13993–14006, 23–29 Jul 2023.
- [17] George Em Karniadakis, Ioannis G Kevrekidis, Lu Lu, Paris Perdikaris, Sifan Wang, and Liu Yang. Physics-informed machine learning. *Nature Reviews Physics*, 3(6):422–440, 2021.
- [18] Nikola Kovachki, Zongyi Li, Burigede Liu, Kamyar Azizzadenesheli, Kaushik Bhattacharya, Andrew Stuart, and Anima Anandkumar. Neural operator: Learning maps between function spaces with applications to pdes. *Journal of Machine Learning Research*, 24(89):1–97, 2023.
- [19] Jae Yong Lee, SungWoong CHO, and Hyung Ju Hwang. HyperdeepONet: learning operator with complex target function space using the limited resources via hypernetwork. In *The Eleventh International Conference on Learning Representations*, 2023.
- [20] Zhijie Li, Wenhui Peng, Zelong Yuan, and Jianchun Wang. Fourier neural operator approach to large eddy simulation of three-dimensional turbulence. *Theoretical and Applied Mechanics Letters*, 12(6):100389, 2022.

- [21] Zijie Li, Kazem Meidani, and Amir Barati Farimani. Transformer for partial differential equations' operator learning. *Transactions on Machine Learning Research*, 2023.
- [22] Zongyi Li, Nikola Borislavov Kovachki, Kamyar Azizzadenesheli, Burigede liu, Kaushik Bhattacharya, Andrew Stuart, and Anima Anandkumar. Fourier neural operator for parametric partial differential equations. In *International Conference on Learning Representations*, 2021.
- [23] Shilong Liu, Yingwen Zhang, Boris A Malomed, and Ebrahim Karimi. Experimental realisations of the fractional schrödinger equation in the temporal domain. *Nature Communications*, 14(1):222, 2023.
- [24] Ilya Loshchilov and Frank Hutter. Decoupled weight decay regularization. In *International Conference on Learning Representations*, 2019.
- [25] Lu Lu, Pengzhan Jin, Guofei Pang, Zhongqiang Zhang, and George Em Karniadakis. Learning non-linear operators via deepoNet based on the universal approximation theorem of operators. *Nature machine intelligence*, 3(3):218–229, 2021.
- [26] Martine Marion and Roger Temam. Navier-stokes equations: Theory and approximation. *Handbook of numerical analysis*, 6:503–689, 1998.
- [27] Leland McInnes, John Healy, Nathaniel Saul, and Lukas Großberger. Umap: Uniform manifold approximation and projection. *Journal of Open Source Software*, 3(29):861, 2018.
- [28] Roberto Molinaro, Yunan Yang, Björn Engquist, and Siddhartha Mishra. Neural inverse operators for solving PDE inverse problems. In *Proceedings of the 40th International Conference on Machine Learning*, volume 202 of *Proceedings of Machine Learning Research*, pages 25105–25139, 23–29 Jul 2023.
- [29] Tian Pan, Yibing Song, Tianyu Yang, Wenhao Jiang, and Wei Liu. Videomoco: Contrastive video representation learning with temporally adversarial examples. In *Proceedings of the IEEE/CVF Conference on Computer Vision and Pattern Recognition*, pages 11205–11214, 2021.
- [30] Adam Paszke, Sam Gross, Francisco Massa, Adam Lerer, James Bradbury, Gregory Chanan, Trevor Killeen, Zeming Lin, Natalia Gimelshein, Luca Antiga, et al. Pytorch: An imperative style, high-performance deep learning library. *Advances in neural information processing systems*, 32, 2019.
- [31] Rui Qian, Tianjian Meng, Boqing Gong, Ming-Hsuan Yang, Huisheng Wang, Serge Belongie, and Yin Cui. Spatiotemporal contrastive video representation learning. In *Proceedings of the IEEE/CVF Conference on Computer Vision and Pattern Recognition*, pages 6964–6974, 2021.
- [32] Zijian Qin, Chao Qian, Lian Shen, Xiaoping Wang, Ido Kaminer, Hongsheng Chen, and Huaping Wang. Superscattering of water waves. *National Science Review*, 10(7):nwac255, 11 2022. eprint: <https://academic.oup.com/nsr/article-pdf/10/7/nwac255/50497393/nwac255.pdf>.
- [33] Md Ashiqur Rahman, Zachary E Ross, and Kamyar Azizzadenesheli. U-NO: U-shaped neural operators. *Transactions on Machine Learning Research*, 2023.
- [34] Maziar Raissi, Paris Perdikaris, and George E Karniadakis. Physics-informed neural networks: A deep learning framework for solving forward and inverse problems involving nonlinear partial differential equations. *Journal of Computational physics*, 378:686–707, 2019.
- [35] Maziar Raissi, Alireza Yazdani, and George Em Karniadakis. Hidden fluid mechanics: Learning velocity and pressure fields from flow visualizations. *Science*, 367(6481):1026–1030, 2020.
- [36] Olaf Ronneberger, Philipp Fischer, and Thomas Brox. U-net: Convolutional networks for biomedical image segmentation. In *Medical Image Computing and Computer-Assisted Intervention–MICCAI 2015: 18th International Conference, Munich, Germany, October 5–9, 2015, Proceedings, Part III 18*, pages 234–241, 2015.
- [37] Jacob H Seidman, Georgios Kissas, Paris Perdikaris, and George J. Pappas. NOMAD: Nonlinear manifold decoders for operator learning. In Alice H. Oh, Alekh Agarwal, Danielle Belgrave, and Kyunghyun Cho, editors, *Advances in Neural Information Processing Systems*, 2022.

- [38] Jifan Shi, Kazuyuki Aihara, and Luonan Chen. Dynamics-based data science in biology. *National Science Review*, 8(5):nwab029, 02 2021.
- [39] Jifan Shi, Kazuyuki Aihara, Tiejun Li, and Luonan Chen. Energy landscape decomposition for cell differentiation with proliferation effect. *National Science Review*, 9(8):nwac116, 2022.
- [40] Nejib Smaoui, Alaa El-Kadri, and Mohamed Zribi. On the control of the 2d navier–stokes equations with kolmogorov forcing. *Complexity*, 2021:1–18, 2021.
- [41] FT Smith. On the high reynolds number theory of laminar flows. *IMA Journal of Applied Mathematics*, 28(3):207–281, 1982.
- [42] Alexander J Smits, Beverley J McKeon, and Ivan Marusic. High–reynolds number wall turbulence. *Annual Review of Fluid Mechanics*, 43:353–375, 2011.
- [43] Eitan Tadmor. A review of numerical methods for nonlinear partial differential equations. *Bulletin of the American Mathematical Society*, 49(4):507–554, 2012.
- [44] Makoto Takamoto, Timothy Praditia, Raphael Leiteritz, Daniel MacKinlay, Francesco Alesiani, Dirk Pflüger, and Mathias Niepert. Pdebench: An extensive benchmark for scientific machine learning. *Advances in Neural Information Processing Systems*, 35:1596–1611, 2022.
- [45] Alasdair Tran, Alexander Mathews, Lexing Xie, and Cheng Soon Ong. Factorized fourier neural operators. In *The Eleventh International Conference on Learning Representations*, 2023.
- [46] Simone Venturi and Tiernan Casey. Svd perspectives for augmenting deepnet flexibility and interpretability. *Computer Methods in Applied Mechanics and Engineering*, 403:115718, 2023.
- [47] Rui Wang, Robin Walters, and Rose Yu. Meta-learning dynamics forecasting using task inference. *Advances in Neural Information Processing Systems*, 35:21640–21653, 2022.
- [48] Xuping Xie, Muhammad Mohebujjaman, Leo G Rebholz, and Traian Iliescu. Data-driven filtered reduced order modeling of fluid flows. *SIAM Journal on Scientific Computing*, 40(3):B834–B857, 2018.
- [49] Zhaoyang Zeng, Daniel McDuff, Yale Song, et al. Contrastive learning of global and local video representations. *Advances in Neural Information Processing Systems*, 34:7025–7040, 2021.
- [50] Rui Zhang, Peiyan Hu, Qi Meng, Yue Wang, Rongchan Zhu, Bingguang Chen, Zhi-Ming Ma, and Tie-Yan Liu. Drvn (deep random vortex network): A new physics-informed machine learning method for simulating and inferring incompressible fluid flows. *Physics of Fluids*, 34(10), 2022.
- [51] David Zwicker. py-pde: A python package for solving partial differential equations. *Journal of Open Source Software*, 5(48):2158, 2020.

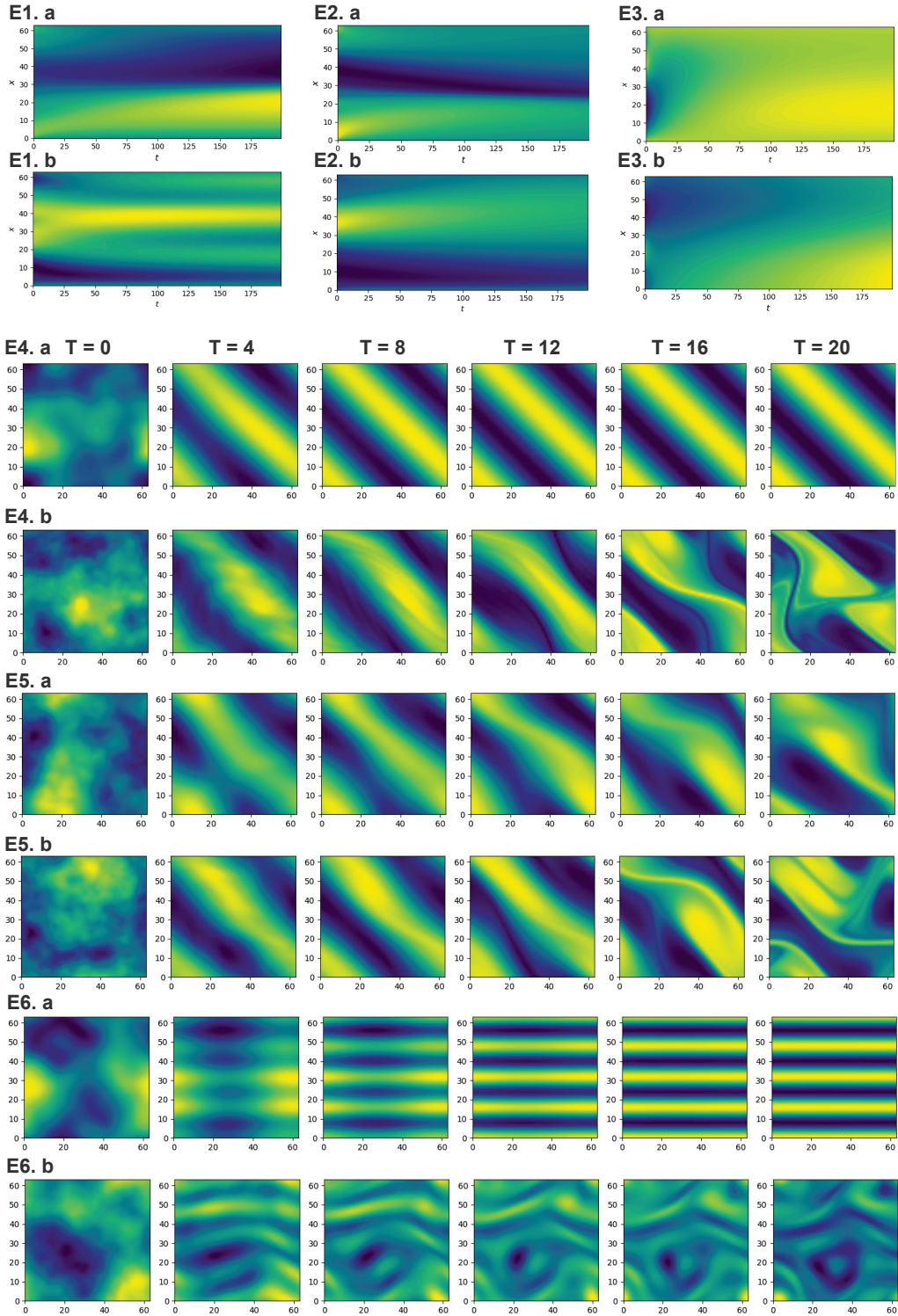


Figure 4: **Examples in the dataset of E1, E2, E3, E4, E5 and E6.** **E1** (Burgers' Equation with varying external forces f). External forces $f(x)$ are set as $-\tanh(3x)$ and $\sin(3x)$ in E1.a and E1.b, respectively. **E2** (Burgers' Equation with varying diffusivities D). The diffusivities $D(x)$ are set as $1 - \cos(x)$ and $1 + \sin(x)$ in E2.a and E2.b, respectively. **E3** (CDE with varying boundary conditions \mathcal{B}). The boundary conditions are set as Dirichlet and Robin in E3.a and E3.b, respectively. **E4** (NSE with varying viscosity terms ν). The viscosity terms ν are set as 10^{-2} and 10^{-5} in E4.a and E4.b, respectively. **E5** (NSE with varying viscosity terms ν and external forces f). The viscosity terms ν and the coefficients in f are set as $(4 \times 10^{-4}, 0.091)$ and $(10^{-4}, 0.135)$ in E5.a and E5.b, respectively. **E6** (Kolmogorov flow with varying viscosity terms ν). The viscosity terms ν are set as 10^{-2} and 10^{-4} in E6.a and E6.b, respectively.

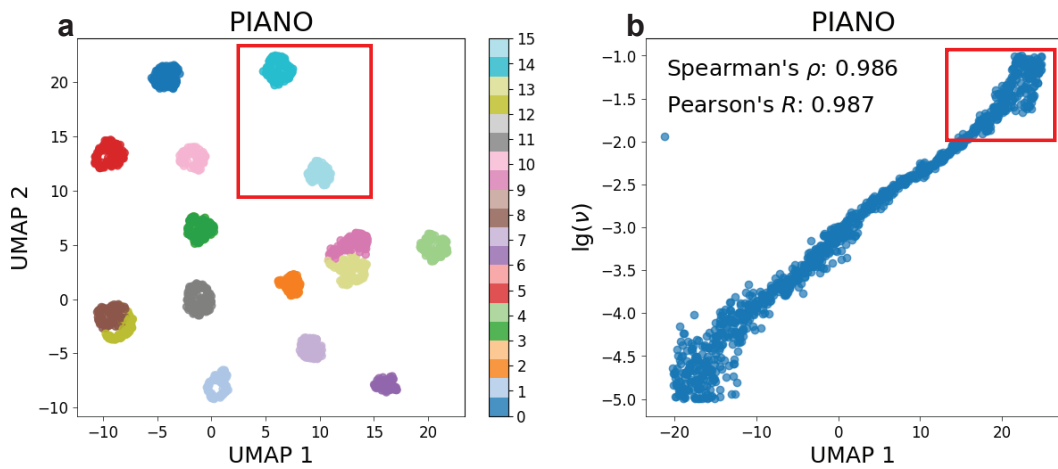


Figure 5: **The out-of-distribution (OOD) generalization ability of the PI encoder.** **a:** The dimensionality reduction results of PI embeddings via UMAP for Burgers' data (E1) are shown. The horizontal and vertical axes represent the two main components of UMAP, and each color represents a different external force in the dataset. The red box encloses the PDE fields driven by the forcing $\sin(4x)$ and $\cos(4x)$, which have never appeared in the training set. **b:** The dimensionality reduction results of the PI embeddings via UMAP for the NSE data (E4) are presented. The horizontal and vertical axes represent the first component of UMAP and the logarithmic viscosity term $\lg(\nu)$ in the dataset. The red box encloses the NSE fields with viscosity terms ranging from 10^{-1} to 10^{-2} , which have never appeared in the training set.

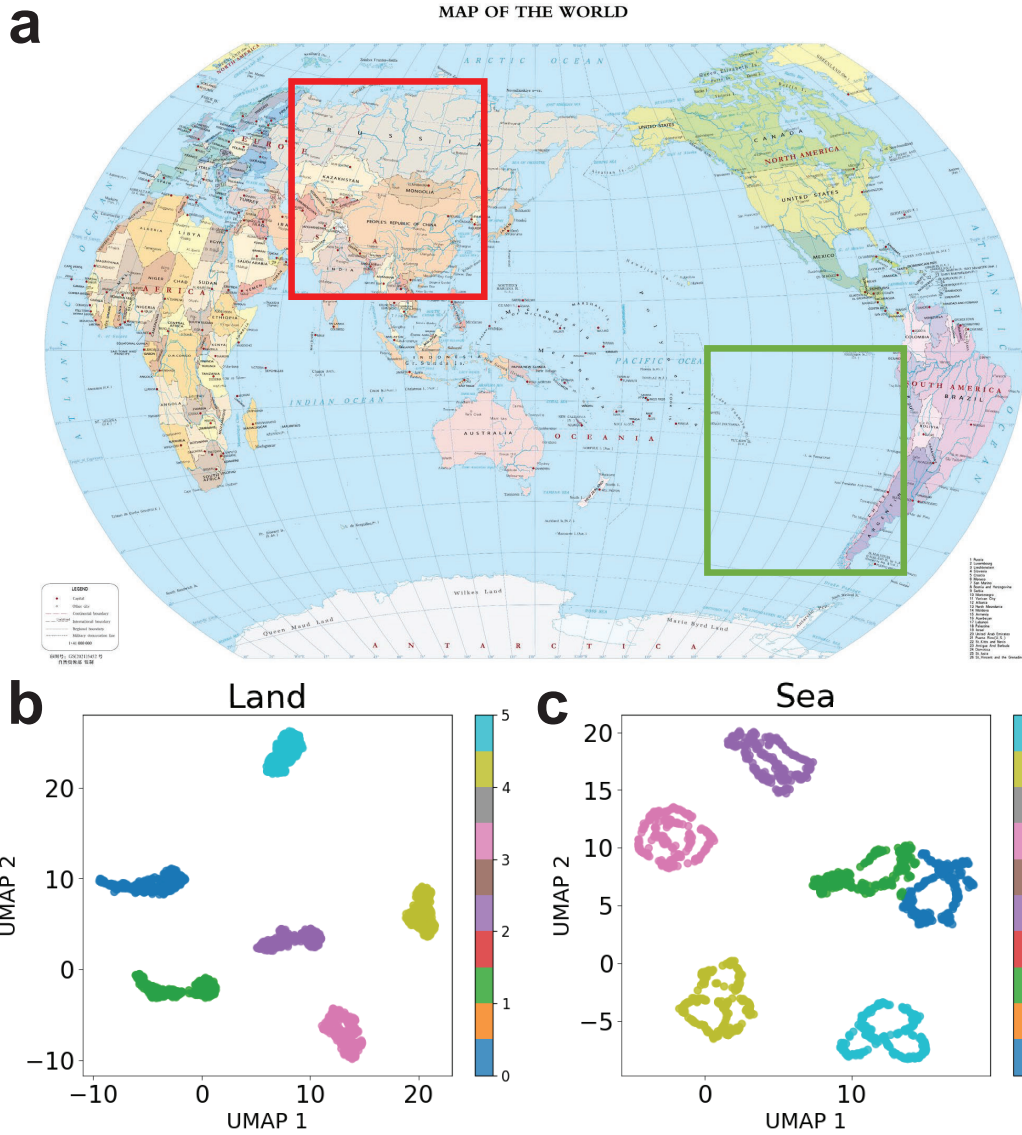


Figure 6: **The performance of the PI encoder in the real-world scenario.** **a**: The geographical locations of the land and sea weather data, which are respectively surrounded by red and green boxes; **b and c**: The dimensionality reduction results of PI embeddings via UMAP for land and sea temperature data, respectively. The horizontal and vertical axes represent the two main components of UMAP, and each color represents a different spatial region in the dataset.